ChemComm

FEATURE ARTICLE

View Article Online
View Journal | View Issue

Cite this: *Chem. Commun.*, 2024, **60**, 5573

Uncovering tetrazoles as building blocks for constructing discrete and polymeric assemblies

Soumya Dey, † Medha Aggarwal,† Debsena Chakraborty and Partha Sarathi Mukherjee *

Received 8th April 2024,
Accepted 30th April 2024

DOI: 10.1039/d4cc01616e

rsc.li/chemcomm

Metal–organic self-assembly with flexible moieties is a budding field of research due to the possibility of the formation of unique architectures. Tetrazole, characterised by four nitrogen atoms in a five-member ring, exhibits immense potential as a component. Tetrazole offers four coordination sites for binding to the metal centre with nine distinct binding modes, leading to various assemblies. This review highlights different polymeric and discrete tetrazole-based assemblies and their functions. The meticulous manipulation of stoichiometry, ligands, and metal ions required for constructing discrete assemblies has also been discussed. The different applications of these architectures in separation, catalysis and detection have also been accentuated. The latter section of the review consolidates tetrazole-based cage composites, highlighting their applications in cell imaging and photocatalytic applications.

1. Introduction

Self-assembly is the process through which multiple components can associate to give an ordered structure. It is like a Lego game where pieces combine to manifest into various

Department of Inorganic and Physical Chemistry, Indian Institute of Science, Bangalore-560012, India. E-mail: psm@iisc.ac.in
† Soumya Dey and Medha Aggarwal contributed equally.

Clockwise from the top left: Partha Sarathi Mukherjee, Medha Aggarwal, Debsena Chakraborty and Soumya Dey

Soumya Dey received his BSc in 2020 from Midnapore College under Vidyasagar University and his MSc in Chemistry in 2022 from IIT Kanpur. He is currently pursuing his PhD at the Indian Institute of Science, Bangalore, under the supervision of Prof. P. S. Mukherjee. His research interests include chiral molecular cages and various chemical reactions under confinement.

Medha Aggarwal received her BSc degree, majoring in chemistry, in 2021 from Doon University and her MS in chemistry in 2023 from the Indian Institute of Science, Bangalore. She is currently pursuing her PhD degree, working with Prof. P. S. Mukherjee at the Indian Institute of Science, Bangalore. Her principal research interests are on stimuli-responsive materials and exploring photophysical and electrochemical aspects of coordination cages.

Debsena Chakraborty received his BSc in 2017 from the University of Burdwan and MS in chemistry in 2019 from the Indian Institute of Science, Bangalore. He is currently pursuing his PhD degree, working with Prof. P. S. Mukherjee at the Indian Institute of Science, Bangalore. His principal research interests concern various applications of water-soluble metal–organic architectures.

Partha Sarathi Mukherjee worked at IACS (Kolkata) for his PhD on magnetic studies of Cu(II) coordination polymers. Subsequently, he worked as a postdoctoral fellow at the University of Utah. He was an Alexander von Humboldt fellow at the University of Göttingen before joining the Indian Institute of Science (IISc) as a faculty in 2005. Partha is currently a professor of chemistry at IISc (Bangalore), where his group is mainly focused on chemistry inside confined space of self-assembled molecular cages. He is a recipient of S. S. Bhatnagar prize and the Swarnajayanti fellowship of the Govt. of India. He is an elected fellow of the Indian Academy of Sciences, and the World Academy of Science (TWAS). Partha is/was in the editorial advisory boards of Inorganic Chemistry, Inorganica Chimica Acta, Inorganic Chemistry Frontiers, The Chemical Records, and Scientific Reports. He is currently serving as an Associate Editor of Inorganic Chemistry.

intricate structures. The self-assembly process is ubiquitous in nature and is found in atomic interactions, cellular replications and in RNA, DNA, and protein folding.[1] Intrigued by the extensive use of self-assembly in nature and the desire to replicate such process in artificial systems, the field of supramolecular chemistry has since then been rapidly developing.

Supramolecular chemistry dates its origin to the discovery of crown ethers, spherands, and cryptands by Pederson,[2] Cram[3] and Lehn,[4] respectively. Lehn defined supramolecular chemistry as the "chemistry beyond the molecule". In other words, it describes how individual species can communicate through various non-covalent interactions (ion–ion, ion–dipole, hydrogen bonding, cation–π, anion–π, π–π, hydrophobic and van der Waals interactions). These interactions help to develop complex structures that can be challenging to construct using conventional covalent chemistry.[5–10] Since the final architecture is made from the association of multiple building blocks, the properties of these blocks are often translated into the final structure.[11–15] This brings us closer to developing artificial analogues of naturally occurring systems.[16,17]

As mentioned earlier, the self-assembly of supramolecular architectures can take place by utilising various interactions. For example, hydrogen bonding is the primary mode of interaction between DNA strands (complementary purine and pyrimidine bases). Rebek and co-workers applied this principle of complementarity to form different hydrogen-bonded capsules.[18,19] Another approach can be the use of electrostatic and aromatic interactions.[20,21] However, the outcome of these electrostatic and aromatic interactions is often unpredictable due to a lack of directionality. This makes it challenging to postulate the consequences, and thus, such interactions are less commonly used to make self-assembled architectures.[22]

Coordination-driven self-assembly is an alternative, robust method that allows predictability and certainty in designing molecular assemblies.[23–25] This approach also has a self-correcting trait due to the dynamic nature of the metal–ligand bonds. This allows concomitant bond cleavage and formation, which leads to the development of thermodynamically stable product(s).[26,27] The coordination-driven self-assembly field has evolved over the years, starting from the seminal work by Lehn[28] and Sauvage[29] to develop metal–organic helicates,[30–32] catenates,[33–35] grids,[36] knots[37,38] and rotaxanes.[39–41] The coordination-driven approach is high-yielding, and the ease of such synthesis has led to the development of a plethora of assemblies.[42] Such assemblies can be either polymeric or discrete, depending on the binding of ligands and metals. Polymeric assemblies mainly constitute coordination polymers (CPs)[43] and their subclass metal–organic frameworks (MOFs).[44] Both CPs and MOFs comprise metal/metal clusters as the node and organic units as the linkers, forming infinite and versatile porous networks. The growth of these polymeric assemblies has been exponential, and such materials have been used in gas adsorption, sensing, and biomedical uses.[45] Nonetheless, these assemblies suffer from a significant drawback of solution-phase processibility due to their low solubility in most polar and non-polar solvents. On the other hand, discrete coordination assemblies, which are comprised of metal–organic cages (MOCs) and metallacycles (MCs), exhibit better solubility in polar and non-polar solvents.[46–49] These structures have diverse applications ranging from catalysis,[50–57] selective separation,[58–62] fluorescence tuning,[63–68] sensing,[69–71] to photochromism.[72,73]

Most self-assembled coordination assemblies use pyridines, carboxylates and imidazoles as the primary linking motifs to the metal centres. All these motifs provide a rigid mono- or bi-dentate binding site. The architectures developed by these motifs using coordination self-assembly are generally predictable and lead to the formation of only a certain number of structures.[74] Tuning the motif using ligands with additional donor sites can open new possibilities for constructing unprecedented structures. This makes tetrazoles a prime candidate for the formation of unusual structures.

Tetrazole is a five-membered aromatic heterocyclic ring with 6-π electrons. It consists of four nitrogen atoms and one carbon atom, where all the nitrogen atoms are linked contiguously. Tetrazoles exist in two tautomeric forms (Fig. 1), where 1*H* is predominant in the solution state, and 2*H* tautomer predominates in the gaseous phase.[75] They are a class of stable heterocycles with the most contiguous nitrogen atoms (as pentazoles are explosive even at low temperatures). The tetrazole motif possesses important traits in terms of low basicity, low pK_a values, higher nitrogen count, high formation enthalpy, good stability, high dipole moment and the presence of a mobile N–H hydrogen donor. These properties have led to the fusion of tetrazoles in profuse applications such as antihypertensive drugs, energy materials, efficient anticancer and antitumour agents, starting materials for propellants, analytical reagents in material science, and as ligands in organisation of complexes. Tetrazoles are bioequivalent of carboxylic acid due to their metabolic stability, so they are also a valuable substitute in drug designs.[76]

The development of tetrazole-based ligands has been a fascinating topic because of their strong coordination abilities. The four nitrogens of tetrazole have four lone pairs oriented in different directions, which provides diversity in binding. Tetrazole can participate in nine diverse binding modes (Fig. 2), including monodentate (two modes), bidentate (four modes), tridentate (two modes) and a tetradentate mode.[77] Tetrazole can act as a multidentate or bridging ligand, depending on the modes. The nitrogen atom of tetrazole can also bind to metal as a neutral ligand or anionic ligand through the deprotonation of the N–H bond.

This review will focus on the use of tetrazoles as the building units. The aim is to highlight the binding affinity of tetrazole to

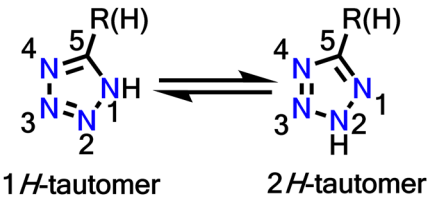

Fig. 1 The two stable tautomers of tetrazole.

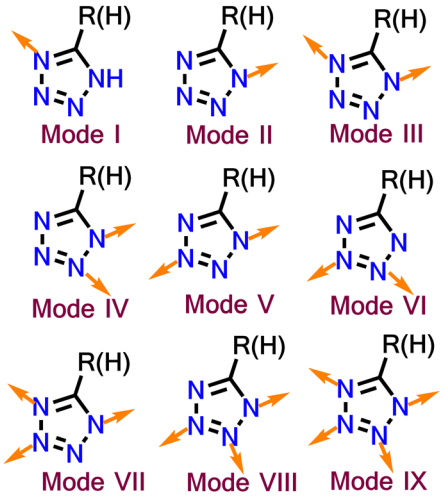

Fig. 2 Different possible binding modes of tetrazole.

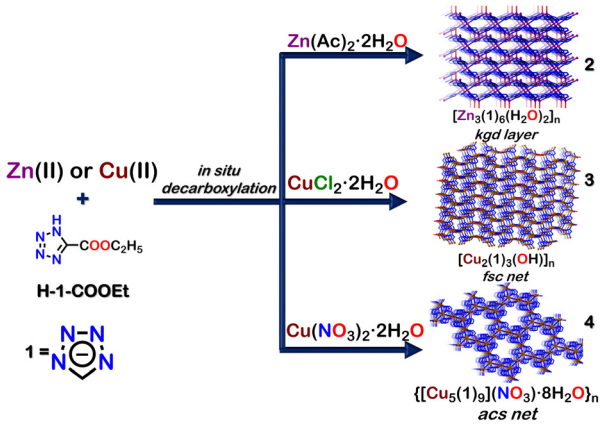

Fig. 3 Schematic representation for the formation of coordination polymers **2** (*kgd* layer), **3** (*fsc* net) and **4** (*acs* net). Crystal structures of **2**,**3**,**4** obtained from ref. 83 [color code: blue, N; black, C; brown, Cu; purple, Zn (H atoms and anions omitted for clarity)].

develop molecular assemblies *via* coordination-driven self-assembly. The initial part of the review will present a short discussion on tetrazole-based coordination polymers and their subclass metal–organic frameworks, followed by details on the formation of tetrazole-based discrete assemblies and their various applications.

2. Tetrazole-based polymeric assemblies

The tetrazole core has diverse binding motifs and has often been used to construct polymeric assemblies by bonding with different metal ions. These metal-derived polymeric assemblies belong to the category of "coordination polymers". Coordination polymers (CPs) can form infinite 1D chains, 2D sheets or 3D networks composed of metal ions/clusters and organic ligands connected *via* coordination bonds.[78] MOFs (metal–organic frameworks) are a subclass of coordination polymers with well-defined pores or voids.[79,80] The scope of tetrazole-based CPs has been discussed in other reviews.[77,80,81] Thus, this review will only provide a glimpse of the use of tetrazole in polymeric assemblies (CPs and MOFs), detailing a few unique examples and applications.

In the first example, Zhong *et al.* showed the formation of different coordination polymers (CPs) with distinct topologies using the reaction of Cu(II) or Zn(II) salt and ethyl tetrazolate-5-carboxylate (**H-1-COOEt**). This reaction resulted in the formation of three CPs $[Zn_3(\mathbf{1})_6(H_2O)_2]_n$ (**2**), $[Cu_2(\mathbf{1})_3(OH)]_n$ (**3**), and $\{[Cu_5(\mathbf{1})_9](NO_3)_3{\cdot}8H_2O\}_n$ (**4**) (Fig. 3). The tetrazolate ligand **1** was generated by an *in situ* decarboxylation reaction of **H-1-COOEt**.

Coordination polymer **2** ($[Zn_3(\mathbf{1})_6(H_2O)_2]_n$) had a rare Kagome dual 2D topological layer structure. In this polymer, the tetrazolate ligand **1** displayed a bidentate nature with mode III (Fig. 2) binding in the network. Coordination polymer **3** had a different 3D pillared layered structure with *fcs* topology net. The ligand **1** showed both bidentate (mode IV) and tridentate (mode VII) binding to the metal (Cu(II)) centre. The coordination polymer **4** exhibited a 3D porous network with *an acs* topology net, and **1** exhibited both tridentate (mode VIII) and tetradentate (mode IX) binding to the metal. Owing to its unique structure, coordination polymer **4** could selectively adsorb CO_2 and H_2 over N_2. Coordination polymer **2**, on the other hand, displayed photoluminescence upon excitation at 292 nm due to LMCT between the zinc centre and the tetrazolate ligand **1**.[82] Similar polymeric materials with other metals like Cobalt (Co(II)) have also been reported.[83]

Micro/nano infinite coordination polymers (ICPs) have recently drawn considerable attention because of their unique physical and chemical properties. Recently, a tetrazole-based ICP was reported to encapsulate TiO_2 and form a distinct kind of ZnO@TiO_2 core–shell structure (Fig. 4). The reaction of $Zn(NO_3)_2{\cdot}6H_2O$ (**5**) with 1,3-bis(tetrazol-5-yl methyl) benzene (**6**), rhodamine B (**7**) and TiO_2 (**8**) in 100 : 100 : 3.3 : 1.25 molar ratio in DMF resulted in the formation of a coordination polymer-dye-nanoparticle composite [**7**/**8**@Zn(**6**)] (**9**). **7** was firmly bound to the surface of TiO_2 due to esterification

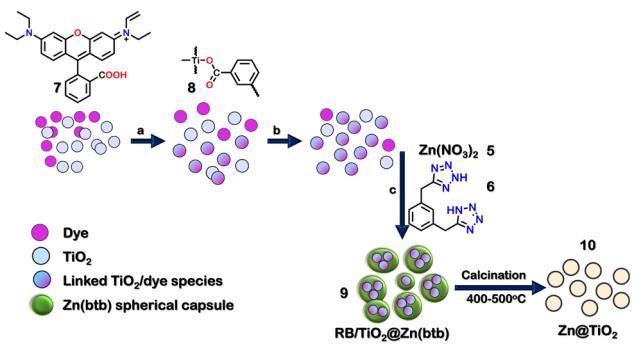

Fig. 4 Schematic representations for the formation of coordination polymer composite RB/TiO_2@Zn(btb) (**9**) [conditions: (a) 5 min sonication, (b) stirring at room temperature for 12 h, (c) methanolic solution of **5** was added with stirring at room temperature].

between the carboxylic group of **7** and the –OH group present on the surface site of TiO_2. The various experimental techniques, such as SEM, HRTEM, EDS, and XRD analyses, confirmed the formation of **9**. It could be used as a template for the synthesis of ZnO@TiO_2 (**10**) core–shell nanoparticles upon calcination between 400 °C and 500 °C.[84]

Tetrazoles can also be used to construct MOFs.[85,86] In 2016, Biswas and co-workers reported the formation of a 3D-amide functionalised Cd(II) MOF with a tetrazole-based organic ligand. This MOF $[Cd_5Cl_6(\mathbf{12})(H\text{-}\mathbf{12})_2]\cdot 7H_2O$ (**13**), (H_2-**12** = 4-(1*H*-Tetrazol-5-yl)-N-[4-(1*H*-tetrazol-5-yl)phenyl]benzamide) (**12**), was synthesised by the reaction of $CdCl_2\cdot H_2O$ (**11**) and **12** in 2 : 1 molar ratio in a DMF–MeOH (1 : 1) solution at 80 °C (Fig. 5(a)). The crystal structure of **13** showed that the ligand **12** acted as a tridentate ligand (*via* mode VIII, Fig. 5(b)). The metal Cd^{2+} (d^{10}-electronic configuration), and π-conjugated electron-rich aromatic ligands endowed **13** with excellent luminescence properties. It was thus used to detect NAEs (nitroaromatic explosives). The steady-state fluorescence titration experiment of activated **13** showed that it could selectively detect 2,4,6-trinitrophenol (TNP) with a detection limit of 1.87×10^{-7} M (42.84 ppb). Gradual fluorescence quenching of **13** was observed with increasing concentration of NAEs with a significantly higher quenching (92%) for TNP. The sensing mechanism revealed that other NAEs were only adsorbed on the surface, while TNP was selectively adsorbed inside the pores of the MOF (**13**) due to proper size matching. UV-visible spectroscopy showed that the absorption band of TNP overlapped with the emission band of **13**, unlike other NAEs, which had almost no overlap. Further, the LUMO of TNP was closer in energy to the HOMO of the ligand **12**, making electron transfer more efficient for TNP than other NAEs. Hence, both the energy and electron transfer mechanisms favoured the highest quenching efficiency of **13** by TNP. Moreover, the recyclability of **13** suggested high photostability and reusability, which made it suitable for detecting explosive materials for a longer duration.[87]

Recently, Huang and co-workers also reported the synthesis of AIE (aggregation-induced emission) active tetrazole-based MOF (**17**). The solvothermal reaction of tetrakis[(4-cyanyl)-phenyl]ethylene (**14**), $CdCl_2\cdot H_2O$ (**11**), and NaN_3 (**15**) in 1 : 3 : 4 molar ratio in a solution of DMA and H_2O resulted in the formation of $\{[Cd_4(\mathbf{16})_2Cl_5]\cdot(N_3)_3\}$ (**17**) (Fig. 6(a)). The crystal structure of **17** displayed the bidentate binding mode (*via* mode VI, Fig. 6(b)) of *in situ* generated ligand **16** ([4-(1*H*-tetrazol-5-yl) phenyl]ethylene). **17** showed excellent AIE properties in the methanol/acetonitrile system with a 16-fold increase in fluorescence quantum yield on going from a non-aggregated state (only methanol solvent) to an aggregated state [90% (v/v) acetonitrile/methanol solvent]. The emulsion of **17** in water was also used for NAE detection. **17** was able to detect TNP selectively over other NAEs with a detection limit of 6.023×10^{-8} M through fluorescence quenching.[88] Other groups have also reported different tetrazole-based luminescent MOFs, which exhibit different applications.[89–91]

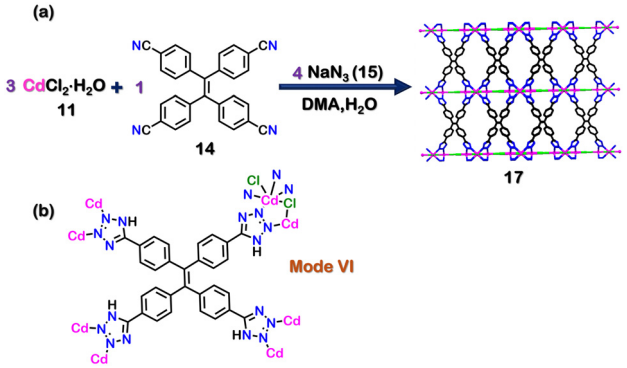

Fig. 6 (a) Schematic representation for the formation of **17**. Crystal structure of **17** obtained from ref. 88 [color code: blue, N; black, C; magenta, Cd; green, Cl; (H atoms and anions omitted for clarity.)] (b) Binding mode of ligand **16**.

The central utility of MOFs lies widely in gas adsorption and its capability for selective separation of gases.[92–95] In 2015, Chen and co-workers reported a microporous MOF (**20**) which was prepared by treating $CuCl_2\cdot 2H_2O$ (**18**) and **19** (5-(5-Amino-1*H*-tetrazol-1-yl)-1,3-benzenedicarboxylic acid) in 1 : 1 molar ratio with HBF_4 in a mixture of DMF–MeOH at 80 °C (Fig. 7(a)). The tetrazole ligand **19** had binding *via* mode III (Fig. 7(b)) in the framework. The crystal structure also confirmed the existence of well-defined pores. Adsorption experiments of N_2 gas on activated **20** showed a surface area of 970 $m^2\ g^{-1}$ and a specific pore volume of 0.399 $cm^3\ g^{-1}$. Owing to these unique pore structures and properties, **20** was used to separate acetylene

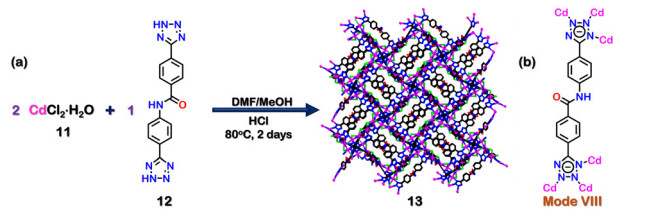

Fig. 5 (a) Schematic representation for the formation of **13**. Crystal structure of **13** was obtained from ref. 87 [color code: blue, N; black, C; magenta, Cd; red, O; green, Cl (H atoms and anions omitted for clarity)]. (b) Binding mode of ligand **12**.

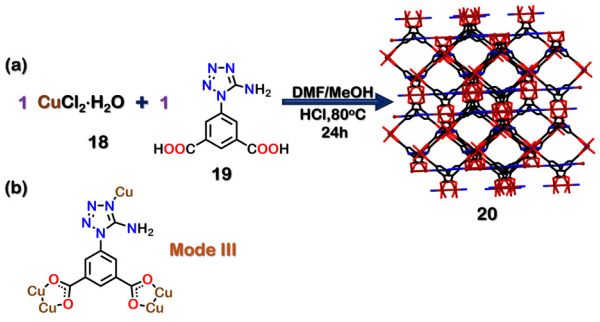

Fig. 7 (a) Schematic representation for the formation of MOF **20**. Crystal structure **20** was obtained from ref. 97 [color code: blue, N; black, C; brown, Cu; green, Cl; red, O (H atoms and anions omitted for clarity.)] (b) Binding mode of ligand **19**.

and ethylene. Such separation is essential because acetylene is an impurity obtained in the industrial production of ethylene *via* the hydrocarbon cracking method. It is necessary to separate acetylene from the mixture of ethylene/acetylene as both pure ethylene and pure acetylene are widely employed as raw chemicals in various industries. Further, the presence of acetylene has detrimental effects on the end products formed from ethylene.[96] The gas sorption isotherm of activated **20** indicated that the uptake ability for acetylene was 95.6 $cm^3\ g^{-1}$, and that of ethylene was 37.2 $cm^3\ g^{-1}$ at 296 K. The uptake ratio was reported as 2.57 from a mixture of acetylene/ethylene. The authors concluded that the availability of a suitable pore size and selective window allowed **20** to display such a high sieving effect and high adsorption selectivity for acetylene over ethylene gas. They also hypothesised that the weak acid–base interactions between the $-NH_2$ groups of the ligand **19** and acetylene molecules also played an essential role in this preferential binding.[97] Co-based mixed tetrazole MOFs are also known to exhibit similar gas adsorption properties.[98]

Recently, two Co-based isorecticular MOFs, **24** $(Co_3(\mathbf{22})_3(DMF)_3(H_2O)_6)$ and **25** $(Co_3(\mathbf{23})_3(DMF)_3(H_2O)_6)$ have been reported. The reaction between $CoCl_2{\cdot}6H_2O$ (**21**) and ligands **22** (2,6-di(1*H*-tetrazol-5-yl)naphthalene) and **23** (2,6-bis(4-(1*H*-tetrazol-5-yl)phenyl)naphthalene) in a 1 : 1 molar ratio in H_2O/DMF led to the formation of **24** and **25**, respectively (Fig. 8(a)). The ligands bind with the Co centre through the tetrazole moiety in a bidentate fashion (*via* mode VI, Fig. 8(b)). The surface area calculated for the activated MOFs **24** and **25** using BET isotherm for N_2 gas was 43.0 $m^2\ g^{-1}$ and 4.47 $m^2\ g^{-1}$, respectively. However, the CO_2-sorption studies with activated **24** showed a Dubinin–Astakhov CO_2-specific surface area of 636 $m^2\ g^{-1}$ and 308 $m^2\ g^{-1}$ for activated **25**. The CO_2 uptake for **24** and **25** was 2.35 mmol g^{-1} and 1.31 mmol g^{-1}, respectively. The higher CO_2 uptake compared to that of N_2 was attributed to the presence of the tetrazole motifs, which display strong dipole–dipole and acid–base interactions between the MOFs and CO_2. Moreover, this CO_2 uptake property of **24** was used for the heterogeneous catalysis of tandem epoxidation carboxylation of styrene (Fig. 9). This conversion of CO_2 to a valuable product showed

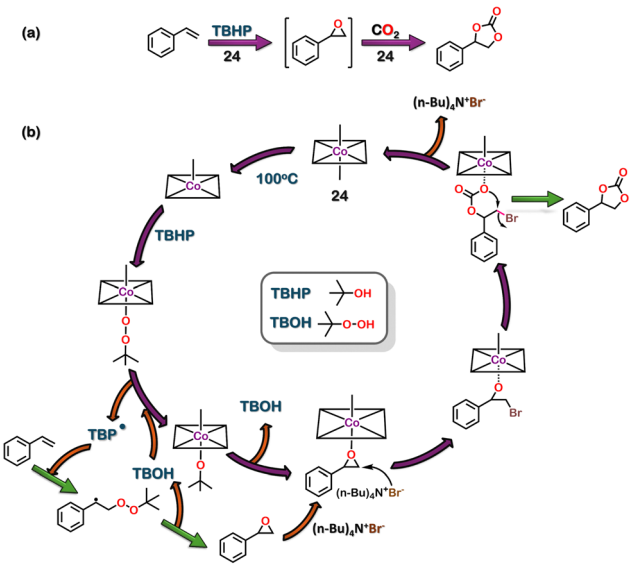

Fig. 9 (a) Reaction scheme for styrene epoxidation followed by cycloaddition. (b) Proposed mechanism.

an excellent approach to tackle the emission of greenhouse gases. This reaction resulted in the formation of cyclic lactones, which are essential chemicals in polymer and pharmaceutical industries.[99] Interestingly, ligand **22** is very versatile and could be used to construct tetrazole-based MOF using other metal units as well.[100]

Using chiral tetrazole ligands, chiral self-assembled structures can also be created. Zhang and co-workers reported a homochiral mixed-valent MOF $\{[Cu_2^{I}Cu^{II}(\mathbf{26})_2(CN^-)(H_2O)]^+[NO_3^-]\}{\cdot}[DMF]$ (**29**) by using an enantiopure ligand **26** ((1*S*)-1-(5-tetrazolyl)-ethylamine). The reaction of **26**, $K_3[Fe(CN)_6]$ (**27**), $Cu(NO_3)_2$ (**28**) and NaOH in the solvent mixture DMF, H_2O and EtOH at 100 °C for two days resulted in the formation of **29** (Fig. 10(a)). The crystal structure of **29** showed a tridentate binding mode of the tetrazole ligand **26** (*via* mode VII, Fig. 10(b)). Since chiral sites can be employed to recognise and separate enantiomers, the ability of **29** to separate chiral alcohols was examined. **29** was able to separate (*R*/*S*)-1-phenyl ethanol and (*R*/*S*)-1-phenyl propanol with a moderate ee (enantiomeric excess) of 42% and 48%, respectively, favouring the *R*-isomers.

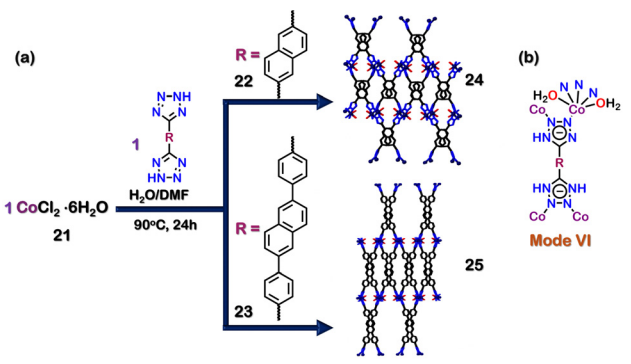

Fig. 8 (a) Schematic representation for the formation of **24** & **25**. Crystal structures of **24** and **25** were obtained from ref. 99 [color code: blue, N; black, C; violet, Co; green, Cl; red, O (H atoms and anions omitted for clarity.)] (b) Binding mode of ligands **22** & **23**.

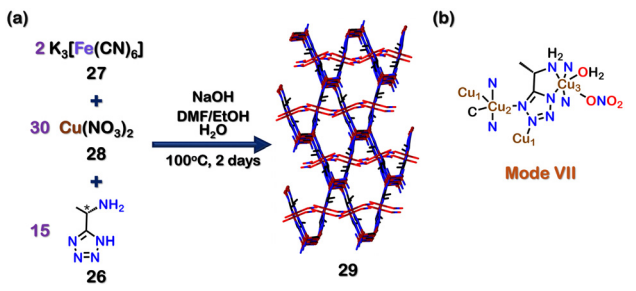

Fig. 10 (a) Schematic representation for the formation of MOF **29**. Crystal structure of **29** was obtained from ref. 101 [color code: blue, N; black, C; red, O; brown, Cu (H atoms and anions omitted for clarity.)] (b) Binding mode of ligands **24** & **25**.

The interactions (hydrogen-bonding, π–π, and stereochemical interactions) between the chiral surface of the MOF and the chiral carbon were mainly responsible for separating the enantiomers.[101]

3. Tetrazole-based discrete assemblies

As seen in the previous section, most of the applications of polymeric assemblies are related to the separation of fluids using amorphous/crystalline solids[99,101] or as an emulsion in different solvents.[88] These polymeric architectures suffer from solution processibility, significantly limiting their applications. To tackle this hardship, other discrete self-assembled architectures soluble in organic and polar solvents are needed. The diversity in binding modes of tetrazole often leads to the formation of polymeric assemblies. However, precise mapping of the coordination sites is vital to forming discrete assemblies, which makes such systems rare. The preference of different metal ions towards different binding modes has been detailed in Table 1. This section will discuss such assemblies and their uses in detail.

In 2015, Stang and coworkers reported the selective formation of four self-assembled molecules through stoichiometric control. The combination of metal acceptor [(*p*-cymene) $RuCl_2]_2$ (**30**), ligand (5-(2-hydroxyphenyl)-1*H*-tetrazole) (**31**) and silver triflate (**32**) in different ratios formed different homometallic and heterometallic architectures (Fig. 11(a)). The combination of **30**, **31** and **32** in an equimolar ratio led to formation of 1D homometallic complex (**33**). When **30**, **31** and **32** were combined in a 3 : 4 : 12 ratio, a 2D rectangular macrocycle (**34**) was formed. In the complex (**33**), ligand **31** acted as a bridging ligand (mode VI, Fig. 2) by binding in a bidentate (Fig. 11(b)) fashion through μ_2-mode. In **34**, the ligand **31** also coordinates in a bidentate fashion but *via* mode V, thus forming a new assembly **34**. **34** contains two types of Ru centres. Four Ru(II) centres form the rectangle by coordinating with the tetrazole moiety's N and O from the phenyl ring. The remaining two Ru centres coordinate to the η^6-of the benzene ring (Fig. 11(b)). The tetrazole moiety of ligand **31** in the dimer (**33**) and rectangle (**34**) still contained free N-atoms with a lone pair of electrons. Adding additional metal ions enabled the tetrazole motif to utilise these binding sites. The introduction of excess silver in a ratio of 1 : 2 : 6 and 3 : 6 : 20 resulted in two new heterometallic 3D architectures (**35**, **36**). In a rare mode, both **35** and **36** utilised **31** as a tetradentate ligand (*via* mode IX, Fig. 2). The attainment of mode IX of tetrazole in a discrete assembly without polymer formation was noteworthy. Compound **35** had a cylindrical shape consisting of 6 Ru centres,

Table 1 Outline of metal ions with their preferential binding modes with tetrazoles in discrete metal–organic cages

No.	Metal ion	Preferred binding mode during cage formation [Ref.]
1	Ru^{2+}/Ag^{1+}	VI, V, IX[102]
2	Pd^{2+}	V,[103,105,106] VI[106]
3	Ir^{2+}	IV, V, VI[104]
4	Eu^{3+}, Gd^{3+}, Tb^{3+}	II[107]
5	Co^{2+}/Fe^{2+}	VI[108]

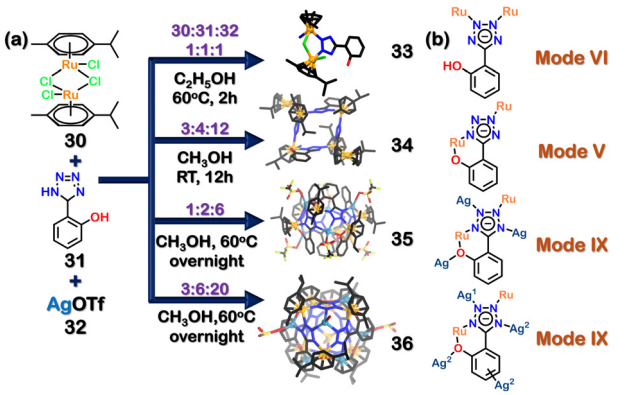

Fig. 11 (a) Schematic representation of the formation of the homometallic dimer (**33**) and 2D-rectangle (**34**), heterometallic cylinder (**35**) and double cone (**36**). Crystal structures of **33**, **34**, **35**, and **36** were adopted from ref. 102 [color code: blue, N; black, C; orange, Ru; pale blue, Ag (H atoms and anions omitted for clarity.)] (b) Representation of multiple binding modes of **31**.

6 Ag ions and 6 ligands (Fig. 11(b)). The new heterometallic cylinder (**35**) allows Ru and Ag to bind in a tetra-coordinated fashion. The second heterometallic structure **36** was a double cone architecture due to the presence of excess Ag ions. The binding of the Ru centres was similar to that in **35**; the only difference lied in the additional Ag ions in **36**. The double cone architecture **36** consists of two types of Ag ions. One type of Ag was bonded to the ligand (**31**), whereas the other type bonded to the benzene ring (Fig. 11(b)). This study demonstrated the importance of binding modes in determining the structure of the final assembly. It also showed the dependence of the tetrazole moiety on stoichiometry and the relative abundance of metal centres.[102]

Mukherjee and co-workers reported two water-soluble tetrahedral nano-cages with tetrazolate ligands (Fig. 12(a)). The combination of 1,4-di(1*H*-tetrazol-5-yl) benzene (**37**) and 1,3,5-tri(1*H*-tetrazol-5-yl) benzene (**38**) with *cis*-(tmeda)$Pd(NO_3)_2$

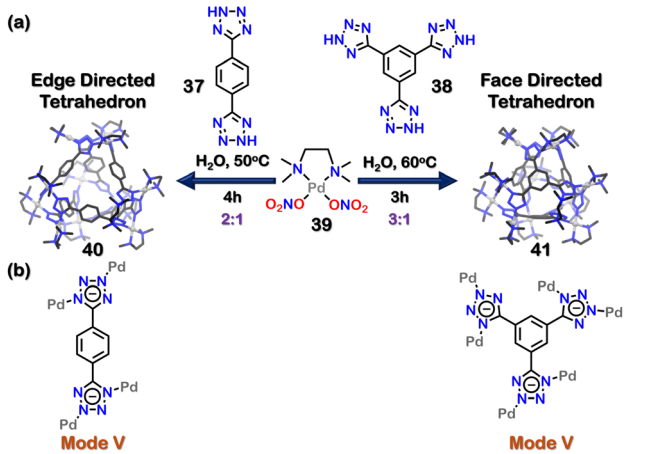

Fig. 12 (a) Schematic representation of the formation of tetrahedron cages (**40**, **41**). Crystal structures of **40**, **41** reproduced from ref. 103 [color code: blue, N; black, C; grey, Pd (H atoms and anions omitted for clarity.)] (b) Binding modes of **37** and **38**.

[tmeda = *N*,*N*,*N*′,*N*′-tetramethylethane-1,2-diamine] (**39**) in 1 : 1 and 3 : 2 molar ratios in water or DMSO formed soft metallogels. The formation of metallogels (a form of polymeric assembly) arose due to the versatile binding nature of the tetrazole motif.

However, when the ratio of **37** to *cis*-(tmeda) $Pd(NO_3)_2$ (**39**) was changed to 1:2 , a discrete edge-directed tetrahedral cage **40** was obtained. In this cage, ligand **37** occupied the edges of a tetrahedron and the corners were made of three tetrazole moieties connected to three *cis*-(tmeda)$Pd(NO_3)_2$ units. The ligand **37** bonded to the Pd centres in a bidentate manner (*via* mode V, Fig. 12(b)). Similarly, when the ratio of ligand **38** to acceptor *cis*-(tmeda)$Pd(NO_3)_2$ was changed to 1 : 3, a discrete face-directed tetrahedral cage (**41**) was formed. In **41**, ligand **38** occupied the tetrahedron's 4 faces, and the corners were formed by bonding three tetrazole moieties with three acceptor units. The denticity and binding mode for ligand **38** were the same as that observed in ligand **37**. The unique 1,3-binding mode (mode V, Fig. 12(b)) of tetrazole moieties with the acceptor units imparted helicity to the tetrazole cages. These corners could be characterised as either a right-handed (Δ) or a left-handed (Λ) helix. As there were four corners in cages **40** and **41**, multiple diastereomeric and/or isomeric cages could be formed (Fig. 13). The crystal structure showed the formation of both (ΛΛΛΛ) or (ΔΔΔΔ) cages, making the system overall achiral through racemisation.[103]

Further, **40** had a hydrophobic cavity with open windows. Thus, it was employed as a host to perform reactions inside its cavity. **40** successfully catalysed Michael's addition reactions of water-insoluble nitro-olefins with 1,3-dimethyl barbituric acid (Fig. 14).[103]

Changing the metal centre and the orientation of the ligand can also lead to the formation of different architectures. Lee and coworkers used half-sandwich iridium (Ir) complexes and three tetrazole ligands to synthesise three novel architectures (Fig. 15(a)). The combination of $[Cp^*IrCl_2]_2$ (**41**), di-tetrazole ligand (**42**), and Ag(OTf) (**43**) in a molar ratio of 1 : 1 : 3 resulted in the formation of a tetranuclear architecture (**44**). The tetranuclear rectangular architecture (**44**) had four Ir centres coordinated to two ligands (**42**), and a Cl atom bridged between two Ir centres. The tetrazole motif displayed two distinct bidentate modes (mode V and mode VI) (Fig. 15(b)). Interestingly, ligand **42** was an isomer of ligand **37**, which was previously used to make tetrahedral cages. This showed how changing the ligand

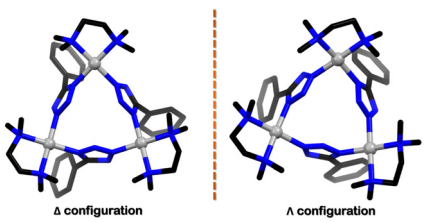

Fig. 13 Representation of a right-handed (Δ) configuration and a left-handed (Λ) configuration present in one edge of the tetrahedron **40**, formed through the coordination of metal centre (**39**) and tetrazole ligands (**38**).

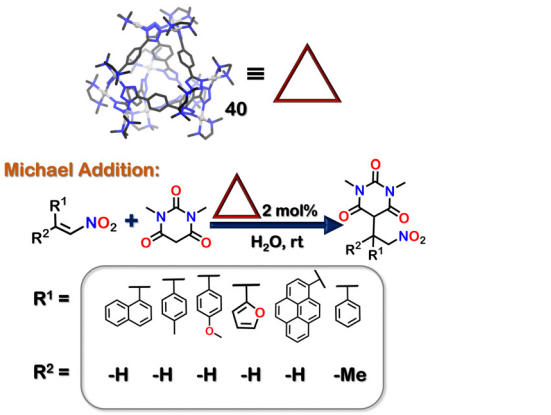

Fig. 14 Michael addition reaction of insoluble nitro olefins facilitated by the tetrahedron cage **40**.

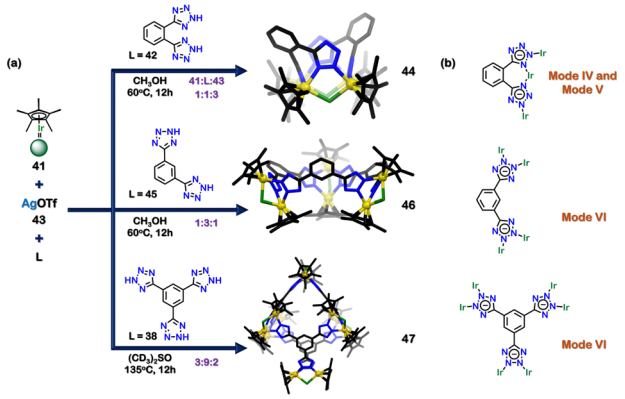

Fig. 15 (a) Schematic representation for the formation of tetranuclear rectangular architecture (**44**), hexanuclear supramolecule architecture (**46**) and dodecanuclear supramolecular architecture (**47**). Crystal structures of **44**, **46** and **47** were adopted from ref. 104 [color code: blue, N; black, C; golden, Ir (H atoms and anions omitted for clarity)] (b) Representation of binding modes of **42**, **45** and **38**.

structure and metal centre can lead to the formation of diverse architectures.[104]

The combination of **41**, **43** and isomeric di-tetrazole ligand (**45**) in a ratio of 1 : 3 : 1 resulted in the synthesis of a truncated trigonal pyramidal hexanuclear supramolecule architecture (**46**). All the tetrazole motifs indicated a bidentate nature with VI binding mode (Fig. 2 and 15(b)). The composition of the hexanuclear complex consisted of six Ir centres and three ligands (**45**); and a Cl atom bridged between two Ir centres. The isomeric ligands **42** and **45** resulted in the construction of 2D complexes. To develop a 3D architecture, a tridentate ligand (**38**) was introduced. The mixture of **41**, **38**, and **43** in a molar ratio of 3 : 2 : 9 resulted in a 3D dodecanuclear octahedral cage (**47**). This 3D architecture had a truncated octahedral geometry with twelve half-sandwich Ir units and four ligands (**48**); a Cl atom bridged between two Ir centres. The tetrazole ligand displayed a bidentate nature (*via* VI binding mode) (Fig. 15(b)).[104]

Interestingly, the previous example used the same ligand (**38**) with *cis*-blocked Pd-metal to form a tetrahedral cage.[103]

Changing the metal acceptor from Pd to Ir caused the binding modes to change, forming an octahedral cage instead of a tetrahedral one.[104]

Previous reports showed the formation of achiral or racemic cages based on tetrazole moieties. However, tetrazole ligands can also easily fabricate chiral self-assembled architecture. A series of enantiopure homochiral tetrahedral cages by employing chiral enantiopure square planar Pd(II) acceptors ((*R*,*R*)/(*S*,*S*)(N^1,N^1,N^2,N^2-tetramethylcyclohexane-1,2-diamine)Pd(NO_3)$_2$) with di-tetrazole linkers were reported. The combination of 1,4-di(1*H*-tetrazol-5-yl) benzene (**37**) with (*R*,*R*)-Pd(II) acceptor (**48**) in a 1 : 2 molar ratio formed homochiral cage **49** with (ΛΛΛΛ) configuration (Fig. 16(a)). When enantiomeric acceptor (*S*,*S*) (**48**) was used, it formed the other enantiomer with (ΔΔΔΔ) configuration. The tetrazole linker displays bidentate coordination *via* mode V (Fig. 16(b)). The self-assembly of other bi-tetrazole linkers 2,6-di(1*H*-tetrazol-5-yl)naphthalene (**22**) and 4,4′-di(1*H*-tetrazol-5-yl)-1,1′-biphenyl (**50**) with (*R*,*R*) and (*S*,*S*) (**48**) resulted in the formation of enantiopure water-soluble tetrahedral cages with either (ΛΛΛΛ) **or** (ΔΔΔΔ) configuration respectively.[105]

The nanocages should interact with chiral guests in a specific manner to form diastereomeric host–guest complexes. The tetrahedral cage formed by the self-assembly of 4,4′-di(1*H*-tetrazol-5-yl)-1,1′-biphenyl (**50**) had the largest hydrophobic aperture and was used for selective chiral recognition of the ethyl derivative of (*R*/*S*) BINOL (*R*/*S*-EtB). The (ΛΛΛΛ) configuration showed selectivity towards *R*-EtB, whereas the (ΔΔΔΔ) configuration showed selectivity towards *S*-EtB (Fig. 17).[105]

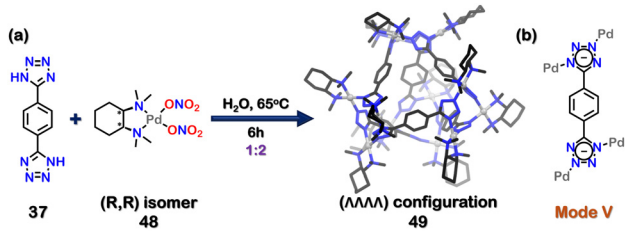

Fig. 16 (a) Schematic representation for the formation of homochiral tetrahedral cage **49**. Crystal structure of **49** is adopted from ref. 105 [color code: blue, N; black, C; grey, Pd (H atoms and anions omitted for clarity)]. (b) Representation of the binding mode of **37**.

Throughout this review, multiple examples of the diverse binding modes of tetrazole to metals have been demonstrated. These bindings are not covalent; thus, switching between these binding modes is possible based on external stimuli. Howlader *et al.* demonstrated that changing the solvent polarity could interchange different molecular architectures. This change caused a dynamic shift between a square-shaped macrocycle and a tetrahedral cage. The binding mode of the tetrazole ligand also changed from mode-VI (in macrocycle) to mode-V (in cage). The self-assembly of di-tetrazole linker **50** [4,4′-bis(1*H*-tetrazol-5-yl)-1,1′-biphenyl] with acceptor (**39**) in 1 : 2 molar ratio in dimethyl sulfoxide (DMSO) and followed by crystallisation, resulted in the formation of a 2D octa-nuclear molecular square (macrocycle) (**51**). All the tetrazole linkers were coordinated in a bidentate manner (*via* mode-VI) (Fig. 18). However, the macrocycle (**51**) was not stable because of the dynamic nature of the metal–ligand bond and the availability of various coordinating sites of tetrazole. Macrocycle **51** transformed into a 3D-tetrahedral cage (**52**), where the di-tetrazole linker transformed its binding mode to V, maintaining a bidentate nature (Fig. 18). This also displays the weaker affinity of binding mode-VI compared to mode-V. The combination of **50** and **39**, along with KPF_6 in a 1 : 2 : 4 molar ratio in less polar acetonitrile solvent, resulted in the formation of a distinct assembly **52** (Fig. 18). The tetrahedral cage **52** also showed transformation to **51** upon introducing a more polar solvent, DMSO. A similar reaction using a triphenyl amine-based tri-tetrazole linker **53** with square planar Pd(II) acceptor **39** in DMSO resulted in the formation of only a 3D-tetrahedral cage **54**, which did not show transformation to macrocycle (Fig. 19). This interconvertible behaviour was unique to the ligand **52** and reluctant to the ligand **53**.[106]

Until now, examples of the self-assembly of tetrazole-based ligands with transition metals of 3d and 4d series have been demonstrated. Generally, the coordination number of these metal ions is restricted to four and six with square planar and octahedral geometries, respectively. The metal ions of the f-block series can be explored to extend the coordination number. The main challenge in designing discrete 4f-series organic polyhedra lies in their complex coordination behaviour, and this absence of precise control could hinder the formation of discrete assemblies. Qing Fu Sun and co-workers

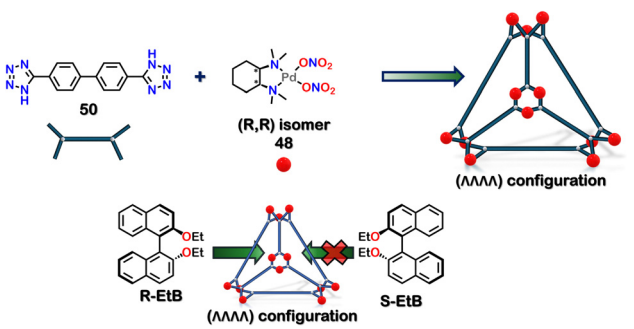

Fig. 17 Illustration to display the selective encapsulation of *R*-EtB over *S*-EtB by the homochiral tetrahedron cage with (ΛΛΛΛ) configuration.

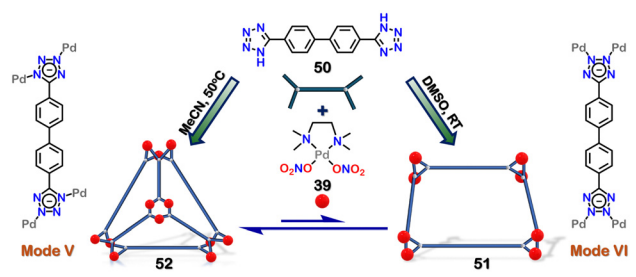

Fig. 18 Schematic representation for the formation of molecular square (**51**) and 3D-tetrahedral cage (**52**) and the dynamic reaction between **51** and **52**, along with the representation of the dual binding modes adopted by **50**.

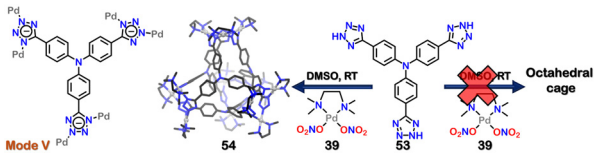

Fig. 19 Schematic representation of distinct 3D-tetrahedral cage (**54**) along with the representation of binding mode of **53**. Crystal structure of **54** was adopted from ref. 106 [color codes: blue, N; black, C; grey, Pd (H atoms and anions omitted for clarity)].

reported a series of water-stable anionic lanthanide organic polyhedra (LOPs) by self-assembling three different bis-tetrazolate ligands and Ln (III) metals. The combination of tetrazolate linker **55** with $Eu(OTf)_3$ in a 3 : 2 molar ratio in DMSO with 12 equivalents of tetraethylammonium hydroxide gave a mixture of $Eu_6(\mathbf{55})_9$ (**56**) and $Eu_4(\mathbf{55})_6$ (Fig. 20(a)). This showed that under the given conditions both the tetranuclear and hexanuclear assemblies were formed and could not be separated. A similar reaction was carried out with $Tb(OTf)_3$ and $Gd(OTf)_3$, which also formed a similar mixture of the final assemblies. However, changing the base to KOH resulted in the discrete formation of **56**. The crystal structure showed that **56** had a trigonal bipyramidal architecture and the tetrazole moiety acted in a monodentate fashion (*via* mode II, Fig. 2). The combination of second tetrazole linker **57** with $Eu(OTf)_3$ in a 3 : 2 molar ratio resulted in the formation $Eu_8(\mathbf{57})_{12}$ cubic structure (**58**) (Fig. 20(a)). Similar structures were formed with $Tb(OTf)_3$ and $Gd(OTf)_3$ metal acceptors. The combination of third linker **59** with other $Ln(OTf)_3$ also formed similar $Ln_8(\mathbf{59})_{12}$ cubic architectures. The combination of **59** along with $EuCl_3{\cdot}6H_2O$ and KOH resulted in the formation of $Eu_{10}(\mathbf{59})_{15}$ architecture, which could be confirmed by mass analysis. The crystallisation, however, led to the transformation of the $Eu_{10}(\mathbf{59})_{15}$ structure to a cubic $Eu_8(\mathbf{59})_{12}$ structure (**60**) (Fig. 20(a)). These Ln(III) based assemblies were stable in aqueous medium due to the electrostatic and chelating interaction between lanthanide metals and ligands. The ligands **57** and **59** also exhibited mode II binding to the metal centre in a monodentate form (Fig. 20(b)). The quantum yield for the cubic structures was obtained for $Tb_8(\mathbf{57})_{12}$ (Φ = 11.2% in water) and $Eu_8(\mathbf{59})_{12}$ (Φ = 76.8% in DMSO). Moreover, the cubic $Gd_8(\mathbf{59})_{12}$ architecture was further employed as an MR (magnetic resonance) imaging contrast agent. Heterometallic cubic assemblies with Eu(III) and Gd(III) could also be created, which showed the dual functionality of luminescent imaging as well as MR imaging.[107]

Discrete architectures could also be constructed using coordination clusters instead of single metal ions at the vertices of the architectures. The incorporation of coordination clusters as the acceptor units form a new class of coordination-cluster cages. Recently, a series of thiacalixarene-based (Co/Fe) coordination clusters were reported to study oxygen evolution reaction (OER). The solvothermal reaction of metal precursors ($CoCl_2{\cdot}6H_2O$ and/or $FeCl_3{\cdot}6H_2O$) along with *p-tert*-butylsulfonylcalix[4]arene (**61**), and 1,3-bis(2*H*-tetrazol-5-yl)benzene (**45**) in a 4 : 1 : 2 resulted in the formation of Co-based coordination cluster (**62**), Fe-based coordination cluster (**63**), and heterometallic Co–Fe coordination cluster (**64**) (Fig. 21(a)). All the clusters were arranged in a box-like fashion where the tetrazole moiety exhibited a bidentate binding (*via* mode VI, Fig. 21(b)). Three bimetallic complexes {CoFe}16-A, {CoFe}16-B (**64**), {CoFe}16-C with different molar ratios were synthesised. The {CoFe}16-B (**64**) cluster was optimised among the three bimetallic clusters to show maximum OER. The synergistic effect in the bimetallic Fe–Co (**64**) cluster helped to study OER with enhanced activity in comparison to **63** and **62**.[108] Such calixarene metal conjugates can also be used for the construction of polymeric systems which can show stimuli dependent chain(polymer) to cage(discrete) transformation.[109]

In the previous examples, tetrazole was used as a ligand, forming coordination bonds with various metals, but such moiety can also be used to functionalize existing metal–organic

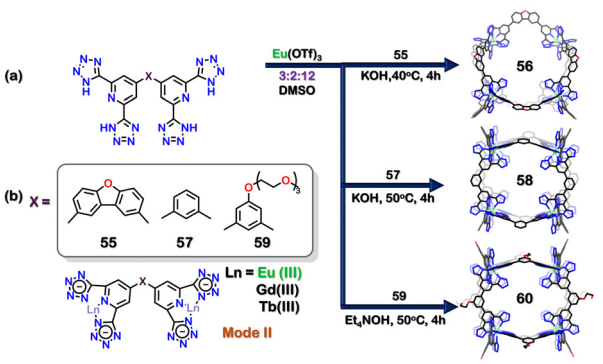

Fig. 20 (a) Schematic representation for the formation of $Eu_6(\mathbf{55})_9$ trigonal pyramidal architecture (**56**), $Eu_8(\mathbf{57})_{12}$ cubic structure (**58**) and $Eu_8(\mathbf{59})_{12}$ architecture (**60**). Crystal structures of **56**, **58** and **60** are adopted from ref. 107 [color codes: blue, N; black, C; red, O; light green, Eu (H atoms and anions omitted for clarity.)] (b) Representation of binding modes of **55**, **57** and **59**.

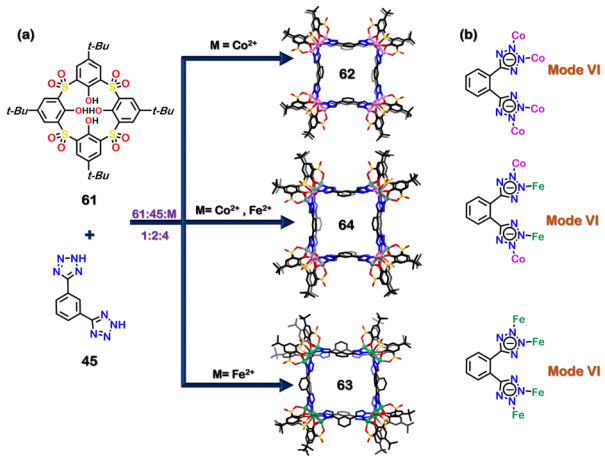

Fig. 21 (a) Schematic representation for the formation of Co-based coordination cluster (**62**), Fe-based coordination cluster (**63**) and heterometallic Co–Fe coordination cluster (**64**). Crystal structures of **62**, **63** and **64** are reproduced from ref. 108 [color code: blue, N; black, C; red, O; yellow, S; dark green, Fe; violet, Co (H atoms and anions omitted for clarity.)] (b) Representation of binding modes of **45**.

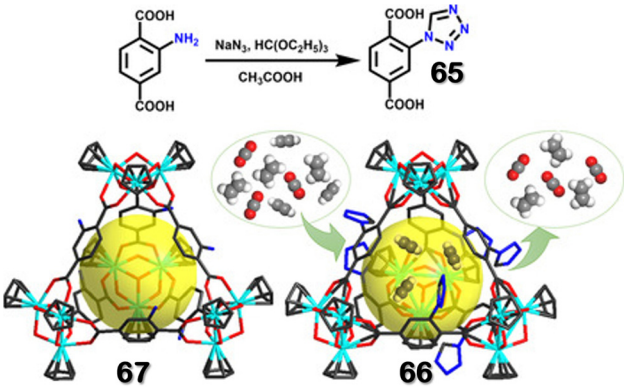

Fig. 22 Schematic representation of the preparation of **65**, along with efficient separation of gases by **66**. Reproduced with permission from ref. 110. Copyright 2021 German Chemical Society.

cages/frameworks. Using the ligand 2-(1*H*-tetrazol-1-yl)terephthalic acid (**65**), synthesis of multiple tetrazole-functionalized MOFs (UiO-66-tetrazole, CAU-1-tetrazole, and MIL-101-tetrazole) have been reported. In these MOFs, the tetrazole unit was free and uncoordinated. Synthesis of a porous metal–organic cage (**66**) by reacting ligand **65** with zirconocene dichloride in a 2 : 5 molar ratio in DMA (Fig. 22) was also reported.

66 had an adsorption capacity of 207.1 $cm^3\ g^{-1}$ and Brunauer–Emmett–Teller (BET) surface area for N_2 gas was calculated to be around 636.7 $m^2\ g^{-1}$. Compared to an amine-functionalized cage (**67**), the tetrazole-functionalised cage showed higher adsorption capability for acidic gases (CO_2, ethylene, and acetylene). The uptake efficiency was based on the order of acidity of the gases. As acetylene (C_2H_2) is more acidic than ethylene (C_2H_4) and CO_2, **66** showed maximum uptake of acetylene and could selectively uptake acetylene (C_2H_2) from the binary mixture of C_2H_2/C_2H_4 and C_2H_2/CO_2. DFT calculation and GCMC simulations elucidated that **66** interacted with the acetylene molecules through hydrogen bonding (*via* $N^{tetrazole}\cdots H\text{–}C$) and the cavity provided sufficient space for multiple dipole–dipole interactions between uptaken acetylene molecules through $C^{\delta+}\cdots H^{\delta-}$, increasing the stability of the host–guest complex. Low heat of adsorption for acetylene, high acetylene uptake capability, and moderate separation selectivity made **66** a suitable candidate for acetylene separation.[110]

3.1 Tetrazole-based cage composites

The lanthanoids are well-established for their distinctive magnetic and optical properties. Due to the highly shielded 4f electrons, lanthanide ions exhibit unique characteristics like sharp emission peaks, long lifetimes, and ligand-independent and environment-independent emission bands. Lanthanide compounds have numerous applications in sensing, bioimaging, luminescent display, and catalysis. However, most reported discrete LOPs and mononuclear lanthanide compounds suffer from inferior water stability, hindering their utilisation in various applications. This section focuses on incorporating lanthanide-based polyhedra (with tetrazole motif) in polymeric networks or porous materials to increase their stability and effectiveness. The utility of these cage composites in different applications has also been briefly discussed.

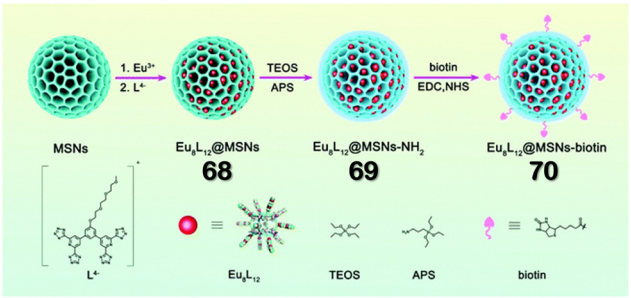

Fig. 23 Schematic representation of the formation of hybrid **70** *via* the employment of a "ship-in-a-bottle" synthetic strategy. Reproduced with permission from ref. 111. Copyright 2022 Royal Society of Chemistry.

Sun and co-workers reported the construction of three cage-composites, namely Eu_8L_{12}@MSNs (**68**) (MSN = mesoporous silica nanoparticles), Eu_8L_{12}@MSNs-NH_2 (**69**) and Eu_8L_{12}@MSNs-biotin (**70**) by employing the "ship-in-a-bottle" strategy. **68** was functionalised to **69** by applying 3-aminopropyl-triethoxysilane (APS). The attachment of biotin on the surface of **68** resulted in the formation of **70** (Fig. 23). The hybrid materials **68**, **69**, and **70** displayed relatively high photoluminescence quantum yields of 38.70%, 40.08%, and 44.04%, respectively. Additionally, **68**, **69** and **70** exhibited better stability than pristine LOP (Eu_8L_{12}). Moreover, the biotin-modified hybrid material **70** revealed excellent cell targeting capability even at a low concentration.[111]

In the second report, different tetrazole-based polyhedra [Gadolinium-based polyhedra ($Gd_8(\mathbf{59})_{12}$)] were employed and encapsulated in MSN (mesoporous silica nanoparticles) by utilising the "ship-in-a-bottle" strategy. The formation of $Gd_8(\mathbf{59})_{12}$@MSN (**71**) was ensured by the reaction of **59** with $Gd(OTf)_3$ in cyclohexane-suspended MSN in a 3 : 10 molar ratio in DMSO solvent (Fig. 24(a)). The solid-state optical Diffuse Reflectance Spectrum (DRS) ascertained **71** as a potential n-type

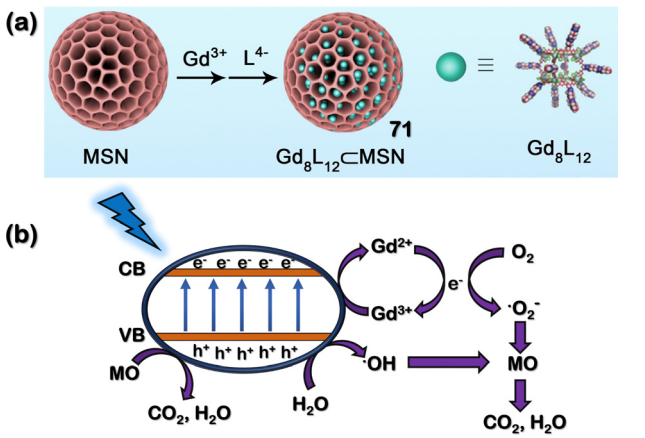

Fig. 24 (a) Schematic representation of the formation of cage-composite **71** *via* the employment of a "ship-in-a-bottle" synthetic strategy. Reproduced with permission from ref. 112. Copyright 2023 Asian Chemistry Editorial Society. (b) Proposed mechanism for the degradation of MO (Methyl Orange) by **71**.

semiconductor due to an optical band gap of 3.40 eV, more prominent than commercially available TiO_2 and other semiconductors. The hybrid material **71** could degrade organic dye methyl orange (MO) under UV irradiation.

It degraded 88.94% of MO (a common macro-pollutant in water) in 2 hours. A plausible mechanism for the photocatalytic degradation of pollutant MO showed the effective generation of electron–hole pairs upon irradiation of UV light (Fig. 24(b)). The reactive holes enabled the formation of hydroxyl radicals, and electron pairs facilitated the formation of superoxide radical anion, which synergistically degraded MO to carbon dioxide and water. Further, **71** demonstrated an affinity for degrading different cationic dyes like MB (methylene blue), RhB (rhodamine-B) and neutral NR (Nile red) under irradiation.[112]

4. Conclusion & outlook

The discipline of coordination-driven self-assembly has significantly expanded in recent decades, owing primarily to its capacity for facile synthesis of intricate architectures surpassing those attainable through traditional covalent chemistry. Notably, the exceptional versatility of tetrazole in adopting nine distinct coordination modes makes it a compelling building block. The initial segment of this review offers a brief overview of tetrazole-based polymeric assemblies, including coordination polymers and their subclass metal–organic frameworks, which have applications in diverse fields such as sensing, gas adsorption and separation, and catalysis.

Subsequently, tetrazole-based discrete assemblies that are soluble in organic and aqueous solvents have been discussed. Precise control over stoichiometry, ligand selection, and metal coordination has facilitated the construction of distinct cages, yielding novel two-dimensional and three-dimensional architectures. These cages have demonstrated utility in catalytic reactions such as Micheal addition and oxygen evolution and have been utilised to design homochiral cages featuring chiral cavities for enantioselective separation. Additionally, discrete cages exhibited gas-separation capabilities, with tetrazole linkers contributing to gas uptake mechanisms. Tetrazole-based LOPs have also emerged as MR contrast agents and luminescent labels. The integration of tetrazole-based lanthanide organic polyhedra (LOPs) into mesoporous silica nanoparticles (MSNs) and their applications in cell imaging and photocatalytic degradation have been highlighted as well.

However, despite the manifold examples of tetrazole-based polymeric assemblies, more investigation into tetrazole linkers for discrete architectures still needs to be done. Thus, many questions on tetrazole-based discrete self-assembly remain unanswered: can tetrazole ligands utilise other binding modes for constructing discrete architecture besides bidentate ones? Can unusual non-platonic architectures or mechanically interlocked structures be fabricated using tetrazole ligands? Can tetrazole or tetrazolium ligands be used to create purely organic cages?

These questions warrant further exploration into the dynamic nature of tetrazole binding modes as the field remains in its infancy. In summation, this review endeavours to consolidate the multifaceted role of the tetrazole motif, advocating for the advancement of tetrazole linker design by incorporating additional functionalities and introducing new applications.

Author contributions

MA and SD have contributed equally to the formulation of the manuscript. DC contributed extensively towards editing the writing and contents of the article, along with a fruitful discussion on tetrazoles. PSM supervised the manuscript and helped in writing the manuscript.

Conflicts of interest

There are no conflicts to declare.

Acknowledgements

We gratefully acknowledge the contributions of the co-workers and colleagues whose names are listed as co-authors in the papers we have cited from our group. S. D. acknowledges UGC for fellowship. D. C. acknowledges PMRF for fellowship. P. S. M. acknowledges SERB (India) for research grant as J. C. Bose fellowship.

References

1 D. Pochan and O. Scherman, *Chem. Rev.*, 2021, **121**, 13699.
2 C. J. Pedersen, *Angew. Chem., Int. Ed. Engl.*, 1988, **27**, 1021.
3 D. J. Cram, *Angew. Chem., Int. Ed. Engl.*, 1988, **27**, 1009.
4 J.-M. Lehn, *Angew. Chem., Int. Ed. Engl.*, 1988, **27**, 89.
5 G. Gupta, Y. Sun, A. Das, P. J. Stang and C. Yeon Lee, *Coord. Chem. Rev.*, 2022, **452**, 214308.
6 J. Zhao, Z. Zhou, G. Li, P. J. Stang and X. Yan, *Natl. Sci. Rev.*, 2021, **8**, nwab045.
7 Z. Yang, F. Esteve, C. Antheaume and J.-M. Lehn, *Chem. Sci.*, 2023, **14**, 6631.
8 M. Zenka, J. Preinl, E. Pertermann, A. Lützen and K. Tiefenbacher, *Eur. J. Inorg. Chem.*, 2023, e202300110.
9 D.-Y. Zhang, Y. Sang, T. K. Das, Z. Guan, N. Zhong, C.-G. Duan, W. Wang, J. Fransson, R. Naaman and H.-B. Yang, *J. Am. Chem. Soc.*, 2023, **145**, 26791.
10 H. Liang, Y. Yang, L. Shao, W. Zhu, X. Liu, B. Hua and F. Huang, *J. Am. Chem. Soc.*, 2023, **145**, 2870.
11 M. Li, Y. Liu, L. Shao, B. Hua, M. Wang, H. Liang, N. M. Khashab, J. L. Sessler and F. Huang, *J. Am. Chem. Soc.*, 2023, **145**, 667.
12 Y.-X. Hu, X. Hao, D. Wang, Z.-C. Zhang, H. Sun, X.-D. Xu, X. Xie, X. Shi, H. Peng, H.-B. Yang and L. Xu, *Angew. Chem., Int. Ed.*, 2024, **63**, e202315061.
13 D. Chakraborty, R. Modak, P. Howlader and P. S. Mukherjee, *Chem. Commun.*, 2021, **57**, 3995.
14 G. Yu, T. R. Cook, Y. Li, X. Yan, D. Wu, L. Shao, J. Shen, G. Tang, F. Huang, X. Chen and P. J. Stang, *Proc. Natl. Acad. Sci. U. S. A.*, 2016, **113**, 13720.
15 M. G. Sullivan, H. K. Welgama, M. R. Crawley, A. E. Friedman and T. R. Cook, *Chem. Mater.*, 2024, **36**, 567.
16 R. A. Tromans, T. S. Carter, L. Chabanne, M. P. Crump, H. Li, J. V. Matlock, M. G. Orchard and A. P. Davis, *Nat. Chem.*, 2019, **11**, 52.
17 W. Liu, Y. Tan, L. O. Jones, B. Song, Q.-H. Guo, L. Zhang, Y. Qiu, Y. Feng, X.-Y. Chen, G. C. Schatz and J. F. Stoddart, *J. Am. Chem. Soc.*, 2021, **143**, 15688.

18 R. Wyler, J. de Mendoza and J. Rebek Jr., *Angew. Chem., Int. Ed. Engl.*, 1993, **32**, 1699.
19 J. Rebek, *Chem. Soc. Rev.*, 1996, **25**, 255.
20 B. Odell, M. V. Reddington, A. M. Z. Slawin, N. Spencer, J. F. Stoddart and D. J. Williams, *Angew. Chem., Int. Ed. Engl.*, 1988, **27**, 1547.
21 H.-Y. Gong, B. M. Rambo, E. Karnas, V. M. Lynch and J. L. Sessler, *Nat. Chem.*, 2010, **2**, 406.
22 D. Chakraborty and P. S. Mukherjee, *Chem. Commun.*, 2022, **58**, 5558.
23 E. G. Percástegui, T. K. Ronson and J. R. Nitschke, *Chem. Rev.*, 2020, **120**, 13480.
24 R. Banerjee, D. Chakraborty and P. S. Mukherjee, *J. Am. Chem. Soc.*, 2023, **145**, 7692.
25 Z. Zhang, L. Ma, F. Fang, Y. Hou, C. Lu, C. Mu, Y. Zhang, H. Liu, K. Gao, M. Wang, Z. Zhang, X. Li and M. Zhang, *JACS Au*, 2022, **2**, 1479.
26 J. Tessarolo, E. Benchimol, A. Jouaiti, M. W. Hosseini and G. H. Clever, *Chem. Commun.*, 2023, **59**, 3467.
27 R.-J. Li, A. Tarzia, V. Posligua, K. E. Jelfs, N. Sanchez, A. Marcus, A. Baksi, G. H. Clever, F. Fadaei-Tirani and K. Severin, *Chem. Sci.*, 2022, **13**, 11912.
28 J.-M. Lehn, *Science*, 2002, **295**, 2400.
29 C. O. Dietrich-Buchecker and J. P. Sauvage, *Chem. Rev.*, 1987, **87**, 795.
30 M.-M. Gan, F. Wang, X. Li, L.-Y. Sun, G. Yuan and Y.-F. Han, *Inorg. Chem.*, 2023, **62**, 2599.
31 Y.-W. Zhao and X.-M. Zhang, *J. Mater. Chem. C*, 2020, **8**, 4453.
32 C. T. McTernan, T. K. Ronson and J. R. Nitschke, *J. Am. Chem. Soc.*, 2021, **143**, 664.
33 N. Hoyas Pérez and J. E. M. Lewis, *Org. Biomol. Chem.*, 2020, **18**, 6757.
34 D. Chakraborty, R. Saha, J. K. Clegg and P. S. Mukherjee, *Chem. Sci.*, 2022, **13**, 11764.
35 G. Gil-Ramírez, D. A. Leigh and A. J. Stephens, *Angew. Chem., Int. Ed.*, 2015, **54**, 6110.
36 J. E. Beves, J. J. Danon, D. A. Leigh, J.-F. Lemonnier and I. J. Vitorica-Yrezabal, *Angew. Chem., Int. Ed.*, 2015, **54**, 7555.
37 D. A. Leigh, F. Schaufelberger, L. Pirvu, J. H. Stenlid, D. P. August and J. Segard, *Nature*, 2020, **584**, 562.
38 H.-N. Zhang and G.-X. Jin, *Angew. Chem., Int. Ed.*, 2023, **62**, e202313605.
39 M. C. Jiménez, C. Dietrich-Buchecker and J.-P. Sauvage, *Angew. Chem., Int. Ed.*, 2000, **39**, 3284.
40 S. Zhang, A. Rodríguez-Rubio, A. Saady, G. J. Tizzard and S. M. Goldup, *Chem*, 2023, **9**, 1195.
41 L. Zhang, Y. Qiu, W.-G. Liu, H. Chen, D. Shen, B. Song, K. Cai, H. Wu, Y. Jiao, Y. Feng, J. S. W. Seale, C. Pezzato, J. Tian, Y. Tan, X.-Y. Chen, Q.-H. Guo, C. L. Stern, D. Philp, R. D. Astumian, W. A. Goddard and J. F. Stoddart, *Nature*, 2023, **613**, 280.
42 R. Saha, B. Mondal and P. S. Mukherjee, *Chem. Rev.*, 2022, **122**, 12244.
43 S. R. Batten, B. Chen and J. J. Vittal, *ChemPlusChem*, 2016, **81**, 669.
44 O. Yaghi and H. Li, *J. Am. Chem. Soc.*, 1995, **117**, 10401.
45 V. J. Pastore and T. R. Cook, *Chem. Mater.*, 2020, **32**, 3680.
46 E. G. Percástegui, J. Mosquera, T. K. Ronson, A. J. Plajer, M. Kieffer and J. R. Nitschke, *Chem. Sci.*, 2019, **10**, 2006.
47 Q. Xu, X. Wang, S. Huang, Y. Hu, S. J. Teat, N. S. Settineri, H. Chen, L. J. Wayment, Y. Jin, S. Sharma and W. Zhang, *Angew. Chem., Int. Ed.*, 2023, **62**, e202304279.
48 B. Moosa, L. O. Alimi, W. Lin, A. Fakim, P. M. Bhatt, M. Eddaoudi and N. M. Khashab, *Angew. Chem., Int. Ed.*, 2023, **62**, e202311555.
49 H.-Y. Lin, Y.-T. Wang, X. Shi, H.-B. Yang and L. Xu, *Chem. Soc. Rev.*, 2023, **52**, 1129.
50 T. Hong, Z. Zhang, Y. Sun, J.-J. Tao, J.-D. Tang, C. Xie, M. Wang, F. Chen, S.-S. Xie, S. Li and P. J. Stang, *J. Am. Chem. Soc.*, 2020, **142**, 10244.
51 C. Ngai, H.-T. Wu, B. da Camara, C. G. Williams, L. J. Mueller, R. R. Julian and R. J. Hooley, *Angew. Chem., Int. Ed.*, 2022, **61**, e202117011.
52 S. Pullen, S. Löffler, A. Platzek, J. J. Holstein and G. H. Clever, *Dalton Trans.*, 2020, **49**, 9404.
53 R. Banerjee, D. Chakraborty, W.-T. Jhang, Y.-T. Chan and P. S. Mukherjee, *Angew. Chem., Int. Ed.*, 2023, **62**, e202305338.
54 S. M. Bierschenk, J. Y. Pan, N. S. Settineri, U. Warzok, R. G. Bergman, K. N. Raymond and F. D. Toste, *J. Am. Chem. Soc.*, 2022, **144**, 11425.
55 D. Chakraborty, S. Ali, P. Choudhury, N. Hickey and P. S. Mukherjee, *J. Am. Chem. Soc.*, 2023, **145**, 26973.
56 V. Martí-Centelles, A. L. Lawrence and P. J. Lusby, *J. Am. Chem. Soc.*, 2018, **140**, 2862.
57 E. O. Bobylev, J. Ruijter, D. A. Poole III, S. Mathew, B. de Bruin and J. N. H. Reek, *Angew. Chem., Int. Ed.*, 2023, **62**, e202218162.
58 L. Catti, R. Sumida and M. Yoshizawa, *Coord. Chem. Rev.*, 2022, **460**, 214460.
59 M. Shuto, R. Sumida, M. Yuasa, T. Sawada and M. Yoshizawa, *JACS Au*, 2023, **3**, 2905.
60 D. Zhang, T. K. Ronson, R. Lavendomme and J. R. Nitschke, *J. Am. Chem. Soc.*, 2019, **141**, 18949.
61 A. Ghosh, J. Pruchyathamkorn, C. Fuertes Espinosa and J. R. Nitschke, *J. Am. Chem. Soc.*, 2024, **146**, 2568.
62 Y. Ding, L. O. Alimi, J. Du, B. Hua, A. Dey, P. Yu and N. M. Khashab, *Chem. Sci.*, 2022, **13**, 3244.
63 M. Ueda, N. Kishida, L. Catti and M. Yoshizawa, *Chem. Sci.*, 2022, **13**, 8642.
64 Y. Hashimoto, Y. Katagiri, Y. Tanaka and M. Yoshizawa, *Chem. Sci.*, 2023, **14**, 14211.
65 S. Zhang, L. Ma, W. Ma, L. Chen, K. Gao, S. Yu, M. Zhang, L. Zhang and G. He, *Angew. Chem., Int. Ed.*, 2022, **61**, e202209054.
66 P.-P. Jia, Y.-X. Hu, Z.-Y. Peng, B. Song, Z.-Y. Zeng, Q.-H. Ling, X. Zhao, L. Xu and H.-B. Yang, *Inorg. Chem.*, 2023, **62**, 1950.
67 J. Gemen, M. J. Białek, M. Kazes, L. J. W. Shimon, M. Feller, S. N. Semenov, Y. Diskin-Posner, D. Oron and R. Klajn, *Chem*, 2022, **8**, 2362.
68 A. Brzechwa-Chodzyńska, G. Markiewicz, P. Cecot, J. Harrowfield and A. R. Stefankiewicz, *Chem. Commun.*, 2023, **59**, 6247.
69 A. B. Sainaba, R. Saha, M. Venkateswarulu, E. Zangrando and P. S. Mukherjee, *Inorg. Chem.*, 2024, **63**, 508.
70 R. Tabuchi, H. Takezawa and M. Fujita, *Angew. Chem., Int. Ed.*, 2022, **61**, e202208866.
71 S. Maji, J. Samanta and R. Natarajan, *Chem. – Eur. J.*, 2024, **30**, e202303596.
72 P. Bhandari, R. Modak, S. Bhattacharyya, E. Zangrando and P. S. Mukherjee, *JACS Au*, 2021, **1**, 2242.
73 A. B. Grommet, L. M. Lee and R. Klajn, *Acc. Chem. Res.*, 2020, **53**, 2600.
74 R. Chakrabarty, P. S. Mukherjee and P. J. Stang, *Chem. Rev.*, 2011, **111**, 6810.
75 U. Bhatt, *Mod. Heterocycl. Chem.*, 2011, 1401.
76 C. G. Neochoritis, T. Zhao and A. Dömling, *Chem. Rev.*, 2019, **119**, 1970.
77 H. Zhao, Z.-R. Qu, H.-Y. Ye and R.-G. Xiong, *Chem. Soc. Rev.*, 2008, **37**, 84.
78 S. R. Batten, N. R. Champness, X.-M. Chen, J. Garcia-Martinez, S. Kitagawa, L. Öhrström, M. O'Keeffe, M. P. Suh and J. Reedijk, *Pure Appl. Chem.*, 2013, **85**, 1715.
79 J. López-Molino and P. Amo-Ochoa, *ChemPlusChem*, 2020, **85**, 1564.
80 X.-M. Kang, M.-H. Tang, G.-L. Yang and B. Zhao, *Coord. Chem. Rev.*, 2020, **422**, 213424.
81 J.-P. Zhang, Y.-B. Zhang, J.-B. Lin and X.-M. Chen, *Chem. Rev.*, 2012, **112**, 1001.
82 D.-C. Zhong, W.-G. Lu, L. Jiang, X.-L. Feng and T.-B. Lu, *Cryst. Growth Des.*, 2010, **10**, 739.
83 H.-F. Wu, J.-G. Xu, J. Lu, F.-K. Zheng, S.-H. Wang and G.-C. Guo, *ACS Omega*, 2019, **4**, 15107.
84 S. Abedi and A. Morsali, *RSC Adv.*, 2015, **5**, 51828.
85 R.-R. Dai, C.-W. Ding, J.-Y. Zhou, R.-J. Wei, X.-Z. Wang, X.-P. Zhou and D. Li, *Inorg. Chem.*, 2021, **60**, 565.
86 B. Abeykoon, J.-M. Grenèche, E. Jeanneau, D. Chernyshov, C. Goutaudier, A. Demessence, T. Devic and A. Fateeva, *Dalton Trans.*, 2017, **46**, 517.
87 A. Buragohain, M. Yousufuddin, M. Sarma and S. Biswas, *Cryst. Growth Des.*, 2016, **16**, 842.
88 P. Gu, H. Wu, T. Jing, Y. Li, Z. Wang, S. Ye, W. Lai, M. Ferbinteanu, S. Wang and W. Huang, *Inorg. Chem.*, 2021, **60**, 13359.
89 T.-W. Tseng, T.-T. Luo, S.-Y. Chen, C.-C. Su, K.-M. Chi and K.-L. Lu, *Cryst. Growth Des.*, 2013, **13**, 510.
90 G.-S. Yang, M.-N. Li, S.-L. Li, Y.-Q. Lan, W.-W. He, X.-L. Wang, J.-S. Qin and Z.-M. Su, *J. Mater. Chem.*, 2012, **22**, 17947.

91 L. Hou, L.-N. Jia, W.-J. Shi, Y.-Y. Wang, B. Liu and Q.-Z. Shi, *Dalton Trans.*, 2013, **42**, 3653.
92 Z. Lu, F. Meng, L. Du, W. Jiang, H. Cao, J. Duan, H. Huang and H. He, *Inorg. Chem.*, 2018, **57**, 14018.
93 P. Cui, Y.-G. Ma, H.-H. Li, B. Zhao, J.-R. Li, P. Cheng, P. B. Balbuena and H.-C. Zhou, *J. Am. Chem. Soc.*, 2012, **134**, 18892.
94 P. Pachfule and R. Banerjee, *Cryst. Growth Des.*, 2011, **11**, 5176.
95 G. Orcajo, G. Calleja, J. A. Botas, L. Wojtas, M. H. Alkordi and M. Sánchez-Sánchez, *Cryst. Growth Des.*, 2014, **14**, 739.
96 H. Molero, B. F. Bartlett and W. T. Tysoe, *J. Catal.*, 1999, **181**, 49.
97 T.-L. Hu, H. Wang, B. Li, R. Krishna, H. Wu, W. Zhou, Y. Zhao, Y. Han, X. Wang, W. Zhu, Z. Yao, S. Xiang and B. Chen, *Nat. Commun.*, 2015, **6**, 7328.
98 J.-Y. Xian, X.-X. Xie, Z.-Y. Huang, Y.-L. Liu, H.-Y. Song, Z.-Q. Chen, Y.-C. Ou and S.-R. Zheng, *Cryst. Growth Des.*, 2023, **23**, 1448.
99 A. Valverde-González, M. C. Borrallo-Aniceto, U. Díaz, E. M. Maya, F. Gándara, F. Sánchez and M. Iglesias, *J. CO2 Util.*, 2023, **67**, 102298.
100 S. Jeong, X. Song, S. Jeong, M. Oh, X. Liu, D. Kim, D. Moon and M. S. Lah, *Inorg. Chem.*, 2011, **50**, 12133.
101 J. Liu, F. Wang, Q.-R. Ding and J. Zhang, *Inorg. Chem.*, 2016, **55**, 12520.
102 Y. J. Park, J. Y. Ryu, H. Begum, M. H. Lee, P. J. Stang and J. Lee, *J. Am. Chem. Soc.*, 2015, **137**, 5863.
103 P. Howlader and P. S. Mukherjee, *Chem. Sci.*, 2016, **7**, 5893.
104 S. G. Lee, J. Y. Ryu, P. J. Stang and J. Lee, *Inorg. Chem.*, 2018, **57**, 8054.
105 P. Howlader, E. Zangrando and P. S. Mukherjee, *J. Am. Chem. Soc.*, 2020, **142**, 9070.
106 P. Howlader, P. Bhandari, D. Chakraborty, J. K. Clegg and P. S. Mukherjee, *Inorg. Chem.*, 2020, **59**, 15454.
107 Z. Wang, L. He, B. Liu, L.-P. Zhou, L.-X. Cai, S.-J. Hu, X.-Z. Li, Z. Li, T. Chen, X. Li and Q.-F. Sun, *J. Am. Chem. Soc.*, 2020, **142**, 16409.
108 X. Hang, X. Wang, M. Wang, M. Chen and Y. Bi, *Inorg. Chem. Front.*, 2023, **10**, 926.
109 X. Zhu, S. Wang, H. Han, X. Hang, W. Xie and W. Liao, *Cryst. Growth Des.*, 2018, **18**, 225.
110 W. Fan, S. B. Peh, Z. Zhang, H. Yuan, Z. Yang, Y. Wang, K. Chai, D. Sun and D. Zhao, *Angew. Chem., Int. Ed.*, 2021, **60**, 17338.
111 X.-S. Lin, Y. Yu, L.-P. Zhou, L. He, T. Chen and Q.-F. Sun, *Dalton Trans.*, 2022, **51**, 4836.
112 X.-S. Lin, W.-H. Liao, L.-P. Zhou and Q.-F. Sun, *Chem. – Asian J.*, 2023, **18**, e202201249.